Citation: Sampaio de Oliveira ML, Uchida TK. Muscle constitutive model with a tangent modulus approximation: Ansys implementation and verification. Journal of Biomechanical Engineering 145(7): 071002, 2023. doi: 10.1115/1.4056948.

Muscle Constitutive Model With a Tangent Modulus Approximation: Ansys Implementation and Verification

Paper Number: BIO-22-1205

Manuel Lucas Sampaio de Oliveira[a], Thomas K. Uchida[a,*]

[a] Department of Mechanical Engineering, University of Ottawa

161 Louis-Pasteur, Ottawa, Ontario, K1N 6N5, Canada

[*] Address all correspondence to this author. E-mail address: tuchida@uottawa.ca

February 15, 2023 – Accepted Manuscript

Abstract

Sophisticated muscle material models are required to perform detailed finite element simulations of soft tissue; however, state-of-the-art muscle models are not among the built-in materials in popular commercial finite element software packages. Implementing user-defined muscle material models is challenging for two reasons: deriving the tangent modulus tensor for a material with a complex strain energy function is tedious and programming the algorithm to compute it is error-prone. These challenges hinder widespread use of such models in software that employs implicit, nonlinear, Newton-type finite element methods. We implement a muscle material model in Ansys using an approximation of the tangent modulus, which simplifies its derivation and implementation. Three test models were constructed by revolving a rectangle (RR), a right trapezoid (RTR), and a generic obtuse trapezoid (RTO) around the muscle's centerline. A displacement was applied to one end of each muscle, holding the other end fixed. The results were validated against analogous simulations in FEBio, which uses the same muscle model but with the exact tangent modulus. Overall, good agreement was found between our Ansys and FEBio simulations, though some noticeable discrepancies were observed. For the elements along the muscle's centerline, the root-mean-square-percentage error in the Von Mises stress was 0.00%, 3.03%, and 6.75% for the RR, RTR, and RTO models, respectively; similar errors in longitudinal strain were observed. We provide our Ansys implementation so that others can reproduce and extend our results.

Keywords: Ansys; elasticity tensor; finite element; hyperelastic material; muscle model; tangent modulus.

1 Introduction

Computational models of skeletal muscle can be used to understand and predict the behavior of muscle during human movement. For example, muscle models have been used to predict the force and stress distribution on the tissues of the lower limb during external compression [1] and to explore why, among the hamstring muscles, the biceps femoris long head is the most susceptible to large strain [2]. Most three-dimensional muscle constitutive models are developed using custom finite element (FE) codes. Models with various levels of complexity have been proposed [3–7], but the difficulty of implementing even simple user-defined muscle models has hindered the widespread adoption of state-of-the-art muscle material models when using commercial software packages. Consequently, research on muscle material models is lacking in general and has suffered from poor reproducibility, both of which have hindered progress in developing new models of skeletal muscle [8].

With the steadily improving processing power of computers, FE models have become popular tools to study muscle behavior. Muscle models can be divided into two broad categories: phenomenological models and biophysical models. Phenomenological muscle models attempt to fit equations to experimental data, without attempting to describe the biological mechanisms by which the observed behaviors emerge. Hill [9] developed the first phenomenological muscle model from experiments that characterized the relationship between the shortening velocity of muscle fibers and the force they produce. This model was later extended into the popular "Hill-type" muscle model commonly used today [10]. In contrast, biophysical muscle models represent the response of muscle by simulating their intrinsic physiological properties [8,11,12]. For example, the underlying aspects of muscle contraction were only understood after Huxley [13] proposed a microstructural model based on the cross-bridge theory. Incorporating the physiological aspects of muscle into a constitutive model can be a complex task. For example, introducing electromechanical dynamics into a hyperelastic material model requires more equations as well as more parameters, both of which increase the complexity of the model [11].

The force generated by muscle is often described as consisting of two components: an active component that depends on the neural activation and a passive component that is independent of activation. Muscles can be simulated using only the passive component if their passive behavior predominates. Linear elastic materials [2], nonlinear hyperelastic materials [14–19], and nonlinear elastic–viscoplastic materials [20] have been used. On the other hand, some simulations require one to consider the effect of muscle activation (e.g., to study the causes of the nonuniform strain in the biceps brachii [6]). The active component of muscle force generation has been considered by introducing an additional term to the strain energy calculation in a hyperelastic transversely isotropic material model [3–6, 21–24]. Another strategy is to mix different element types in a finite element model. For example, Li et al. [25] used solid elements and beam elements to represent the passive and active behavior of muscle, respectively. While popular software packages such as Ansys® and Abaqus® have built-in material models to simulate the passive behavior of muscle (e.g., Neo-Hookean and Mooney–Rivlin models), they lack built-in functions to simulate the active behavior. FEBio, an open-source finite element software package [26, 27], has a built-in muscle model capable of simulating the active component of muscle. Introducing advanced muscle modeling capabilities into Ansys and Abaqus would benefit researchers and engineers as these software packages have many powerful features, broad supporting infrastructure, and large user bases in fields beyond biomechanics. For example, engineers are increasingly interested in virtual prototyping and optimization of robotic devices that interact with the body [28, 29], and Ansys or Abaqus would be a natural choice for designing the robotic components. Providing freely available implementations of sophisticated muscle material models in these software packages would facilitate adoption and accelerate future development.

Muscle material models can be implemented in Ansys and Abaqus by writing a user-defined material subroutine (USERMAT or UMAT, respectively). The Cauchy stress and tangent modulus tensor (also referred to as the elasticity tensor or material Jacobian) are the outputs of these subroutines. The tangent modulus is used as an iterative operator for a Newton-type method to solve initial- and boundary-value problems in FE simulations [30]. For example, the governing equilibrium equations used in finite element methods can be constructed using the principle of virtual work. The resulting nonlinear equations can then be solved using Netwon's method, which involves first linearizing these equations. The second Piola–Kirchhoff stress that appears in the equilibrium equations is linearized using the tangent modulus [30, 31]. USERMAT subroutines also use the tangent modulus associated with the Jaumann rate of the Kirchhoff stress [32]. Computing the Cauchy stress is relatively straightforward because one must calculate only the first derivative of the strain energy and the result is only a second-order tensor (i.e., a matrix). On the other hand, deriving the tangent modulus tensor for a material with a complex strain energy function is tedious because it depends on the second derivative of the strain energy. Furthermore, programming the algorithm to compute the tangent modulus is error-prone because the tangent modulus is a fourth-order tensor and requires one to also implement routines to perform tensor algebra. Additionally, Ansys does not provide extensive tools to support USERMAT development.

Approximation methods have been proposed as an alternative to calculating the tangent modulus. Miehe [33] proposed a forward-difference approximation of the second Piola–Kirchhoff stress to calculate the tangent modulus. Sun et al. [34] proposed an approximation based on the forward difference of the associated Kirchhoff stress by incrementally perturbing the deformation gradient. Tanaka and Fujikawa [35] proposed a higher-order approximation scheme, using the second-order central difference and the complex-step derivative approximation (the latter being a technique to obtain the numerical value of the first derivative using complex arithmetic). All the aforementioned strategies demonstrated good agreement with the exact calculations, but their convergence and accuracy are not guaranteed for all materials and elements [36].

An approximation for the tangent modulus has been applied to several materials, among which are the Neo-Hookean model, Holzapfel's exponential model [34], the Mooney–Rivlin model [35], and the Gasser–Ogden–Holzapfel model [37–40]. However, to the best of the authors' knowledge, an approximation method for the tangent modulus has not yet been applied to a muscle material model. Such an approximation can greatly facilitate the implementation of muscle material models (whose strain energy functions are nontrivial).

In this work, we apply the approximation strategy of Sun et al. [34] to the muscle material model proposed by Blemker et al. [6]. We implement this model as an Ansys user-defined material subroutine. We use several test cases to evaluate the convergence properties and the error in stress and strain when using the approximation. We validate our results through comparison to analogous simulations in FEBio, which uses the same muscle model but with the exact value of the tangent modulus. We provide our Ansys implementation at https://simtk.org/projects/musc_fe_approx so that others can reproduce and extend our results, use the model in their FE simulations, and develop new muscle material models in Ansys more quickly.

2 Methods

For completeness, we begin this section with a summary of some necessary kinematics concepts in continuum mechanics. We then present the formulation to calculate the stress and tangent modulus of a material, which are required to implement a user-defined material model in Ansys. Next, we present the tangent modulus approximation proposed by Sun et al. [34] and the hyperelastic muscle material model proposed by Blemker et al. [6]. Finally, we describe the models and simulations we used to validate our Ansys implementation of this muscle material model with a tangent modulus approximation.

2.1 Kinematics

The deformation gradient ($\mathbf{F}$) is the primary measure of deformation used in nonlinear continuum mechanics:

$$\mathbf{F} = \frac{\partial \mathbf{x}}{\partial \mathbf{X}} \tag{1}$$

where $\mathbf{x}$ is the position in the current configuration (Ω) at a given time t and $\mathbf{X}$ is the position in the reference configuration (Ω_0) [30]. The deformation gradient contains information about the rotational and stretching parts of the deformation. From the deformation gradient, the left ($\mathbf{B}$) and right ($\mathbf{C}$) Cauchy–Green deformation tensors are calculated as follows:

$$\mathbf{B} = \mathbf{F}\mathbf{F}^{\mathrm{T}} \tag{2}$$

$$\mathbf{C} = \mathbf{F}^{\mathrm{T}}\mathbf{F} \tag{3}$$

For materials that are nearly incompressible, such as muscles, the deformation gradient is often decomposed into its volumetric component ($J^{1/3}\mathbf{I}$) and isochoric component ($\bar{\mathbf{F}}$):

$$\mathbf{F} = \left(J^{1/3}\mathbf{I}\right)\bar{\mathbf{F}} \tag{4}$$

where $J = |\mathbf{F}|$ is the volumetric ratio and $\mathbf{I}$ is an identity matrix. Consequently, the left and right Cauchy–Green deformation tensors become $\bar{\mathbf{B}}$ and $\bar{\mathbf{C}}$, respectively, and are expressed as follows:

$$\bar{\mathbf{B}} = J^{-2/3}\mathbf{B} \tag{5}$$

$$\bar{\mathbf{C}} = J^{-2/3}\mathbf{C} \tag{6}$$

2.2 Stress measures

Several stress measures are used in nonlinear problems; the second Piola–Kirchhoff, Cauchy, and Kirchhoff stresses are the most common. The second Piola–Kirchhoff stress ($\mathbf{S}$) is defined from the derivative of the strain energy function (Ψ) with respect to the right Cauchy–Green deformation tensor:

$$\mathbf{S} = 2\frac{\partial \Psi(\mathbf{C})}{\partial \mathbf{C}} \tag{7}$$

For materials that are nearly incompressible, the strain energy is a function of the modified right Cauchy–Green deformation tensor (i.e., $\Psi(\bar{\mathbf{C}})$). Thus, using the chain rule and separating the strain energy into the isochoric and volumetric components, we can calculate the isochoric ($\mathbf{S}_{\text{iso}}$) and volumetric ($\mathbf{S}_{\text{vol}}$) components of the second Piola–Kirchhoff stress as follows:

$$\mathbf{S}_{\text{iso}} = J^{-2/3}\left(\mathbb{I} - \frac{1}{3}\mathbf{C}^{-1} \otimes \mathbf{C}\right) : \bar{\mathbf{S}} \tag{8}$$

$$\mathbf{S}_{\text{vol}} = Jp\mathbf{C}^{-1} \tag{9}$$

where $\mathbb{I}$ is a unit fourth-order tensor; "$\otimes$" and ":" are the tensor product and double-contraction operators, respectively. $\bar{\text{S}}$ is the "fictitious" second Piola–Kirchhoff stress:

$$\bar{\mathbf{S}} = 2\frac{\partial \Psi(\bar{\mathbf{C}})}{\partial \bar{\mathbf{C}}} \tag{10}$$

and p is the hydrostatic pressure:

$$p = \frac{d\Psi_{\text{vol}}(J)}{dJ} \tag{11}$$

The Cauchy and Kirchhoff stresses are calculated using the push-forward operator, which transforms a vector or tensor from the material configuration to the spatial configuration. The Kirchhoff stress ($\boldsymbol{\tau}$) is calculated as the push-forward transformation of the second Piola–Kirchhoff stress (**S**):

$$\boldsymbol{\tau} = \mathbf{F}\mathbf{S}\mathbf{F}^{\mathrm{T}} \tag{12}$$

The Cauchy stress ($\boldsymbol{\sigma}$) is related to the Kirchhoff stress as follows:

$$\boldsymbol{\sigma} = J^{-1}\boldsymbol{\tau} \tag{13}$$

2.3 Tangent modulus and its approximation

Ansys uses a co-rotational frame to express the stress and tangent modulus [32]. Thus, one must use an objective rate of stress to account for the material rotation [38]. Ansys uses the objective Jaumann rate of Cauchy stress ($\overset{\triangledown}{\boldsymbol{\sigma}}$) and the associated tangent modulus ($\mathbb{C}^J$), which is a fourth-order tensor [32]:

$$\overset{\triangledown}{\boldsymbol{\sigma}} = \mathbb{C}^J : \mathbf{D} \tag{14}$$

where $\mathbf{D}$ (the symmetric part of the spatial velocity gradient $\mathbf{L} = \mathbf{F}\mathbf{F}^{-1}$) is the rate-of-deformation tensor. The Jaumann stress rate can also be expressed in terms of the spatial tangent modulus ($\mathbb{C}^S$), the rate-of-deformation tensor ($\mathbf{D}$), and the Cauchy stress ($\boldsymbol{\sigma}$) [39]:

$$\overset{\triangledown}{\boldsymbol{\sigma}} = \mathbb{C}^S : \mathbf{D} + \mathbf{D}\boldsymbol{\sigma} + \boldsymbol{\sigma}\mathbf{D}^{\mathrm{T}} \tag{15}$$

Upon subtracting Eq. (14) from Eq. (15), we find that $\mathbb{C}^J$ can be calculated by adding a term to $\mathbb{C}^S$. The index notation of $\mathbb{C}^J$ is as follows:

$$\mathbb{C}^J_{ijk\ell} = \mathbb{C}^S_{ijk\ell} + \frac{1}{2}\left(I_{ik}\sigma_{j\ell} + \sigma_{ik}I_{j\ell} + I_{i\ell}\sigma_{jk} + \sigma_{i\ell}I_{jk}\right) \tag{16}$$

where i, j, k, and ℓ are the free indices in $\{1, 2, 3\}$. $\mathbb{C}^S$ can be found from the push-forward transformation of the material tangent modulus ($\mathbb{C}$) divided by the volumetric ratio (J):

$$\mathbb{C}^S_{ijk\ell} = J^{-1}F_{iA}F_{jB}F_{kC}F_{\ell D}\mathbb{C}_{ABCD} \tag{17}$$

Finally, $\mathbb{C}$ can be calculated from the second derivative of the strain function:

$$\mathbb{C} = 4\frac{\partial^2\Psi(\mathbf{C})}{\partial\mathbf{C}\partial\mathbf{C}} \tag{18}$$

Deriving the tangent modulus (Eqs. (16) and (17)), a fourth-order tensor, is tedious for a material with a complex strain energy function and programming the algorithm to compute it is error-prone. These challenges can limit the widespread use of state-of-the-art hyperelastic material models. Sun et al. [34] proposed a numerical approximation for the tangent modulus that addresses these challenges. The method of Sun et al. is particularly convenient for the present application as the approximation is performed in the co-rotational frame, which is the frame with respect to which USERMAT outputs must be expressed. The formulation begins by calculating matrices $\Delta\mathbf{F}^{(i,j)}$ for $i, j \in \{1, 2, 3\}$, which are the perturbations of the deformation gradient $\mathbf{F}$ upon perturbing only its (i, j) element:

$$\Delta\mathbf{F}^{(i,j)} = \frac{\epsilon}{2}\left(e_i \otimes e_j\mathbf{F} + e_j \otimes e_i\mathbf{F}\right) \tag{19}$$

where $\epsilon > 0$ is the (small) perturbation parameter and $\{e_1, e_2, e_3\}$ are the basis vectors in the spatial reference frame. Next, the perturbed deformation gradient $\hat{\mathbf{F}}^{(i,j)}$ is computed for each perturbation:

$$\hat{\mathbf{F}}^{(i,j)} = \mathbf{F} + \Delta\mathbf{F}^{(i,j)} \tag{20}$$

The elements of the approximated tangent modulus are then calculated as the forward difference of the Cauchy stress:

$$\mathbb{C}^J_{ijk\ell} = \frac{1}{J\epsilon}\left[J_p^{(i,j)}\boldsymbol{\sigma}\left(\hat{\mathbf{F}}^{(i,j)}\right)_{k\ell} - J\boldsymbol{\sigma}\left(\mathbf{F}\right)_{k\ell}\right] \tag{21}$$

where $J_p^{(i,j)} = \left|\hat{\mathbf{F}}^{(i,j)}\right|$. This approximation has the advantage that Eqs. (19) to (21) are independent of the material model—that is, they depend only on the Cauchy stress, the closed form of which is a required calculation in any Ansys USERMAT subroutine and is, therefore, readily available.

2.4 Hyperelastic muscle material model

We applied the approximation of the tangent modulus proposed by Sun et al. [34] (described in Sec. 2.3) to the hyperelastic muscle material model of Blemker et al. [6]; for completeness, we briefly describe the latter in this section. The isochoric component of the strain energy (Ψ_{iso}) is formed by adding three terms: the along-fiber and cross-fiber shear strain energies (W_1 and W_2) and the muscle fiber stretch strain energy (W_3):

$$\Psi_{\text{iso}}\left(\bar{I}_1, \bar{I}_2, \bar{I}_4, \bar{I}_5, \alpha\right) = W_1\left(B_1\left(\bar{I}_4, \bar{I}_5\right)\right) + W_2\left(B_2\left(\bar{I}_1, \bar{I}_4, \bar{I}_5\right)\right) + W_3\left(\lambda, \alpha\right) \tag{22}$$

where $\bar{I}_1$, $\bar{I}_2$, $\bar{I}_4$, and $\bar{I}_5$ are invariants of the modified right Cauchy–Green tensor ($\bar{\mathbf{C}}$). (Note that muscle is modeled as a nearly incompressible material, hence the use of $\bar{\mathbf{C}}$.) In Eq. (22), functions W_1, W_2, B_1, and B_2 are defined as follows:

$$W_1 = G_1 B_1^2 \tag{23}$$

$$W_2 = G_2 B_2^2 \tag{24}$$

$$B_1 = \sqrt{\bar{I}_5/\bar{I}_4 - 1} \tag{25}$$

$$B_2 = \cosh^{-1}\left(\frac{\bar{I}_1\bar{I}_4 - \bar{I}_5}{2\sqrt{\bar{I}_4}}\right) \tag{26}$$

where G_1 and G_2 are the along-fiber and cross-fiber shear moduli. The volumetric component of the strain energy (Ψ_{vol}) is a function of only the volumetric ratio (J):

$$\Psi_{\text{vol}}(J) = \frac{K}{2}\ln^2(J) \tag{27}$$

where K is the effective bulk modulus. The total strain energy is simply the sum of the isochoric and volumetric components thereof:

$$\Psi = \Psi_{\text{iso}} + \Psi_{\text{vol}} \tag{28}$$

The muscle fiber stretch strain energy (W_3) in Eq. (22) is associated with the Cauchy stress generated by the fiber stretch (σ_{fiber}). W_3 has two components: the passive stress and the active stress. The former depends on the fiber stretch (λ) while the latter depends on both the fiber stretch and the muscle activation (α, where $0 \leq \alpha \leq 1$). It is assumed that all sarcomeres in a fiber have the same length, as do all fibers. The Cauchy stress is related to the strain energy as follows:

$$\lambda\frac{\partial W_3}{\partial \lambda} = \sigma_{\text{fiber}}(\lambda, \alpha) = \sigma_{\text{max}}\frac{\lambda}{\lambda_{\text{opt}}}\left(\mathrm{f}_{\text{passive}}(\lambda) + \alpha\mathrm{f}_{\text{active}}(\lambda)\right) \tag{29}$$

where σ_{max} is the maximum isometric stress, which is the maximum isometric force of the muscle divided by its physiological cross-sectional area, and λ_{opt} is the optimal fiber stretch, which corresponds to the length of the fiber at which the sarcomeres are at their optimal length (i.e., the length at which they can generate the maximum active force). The function $\mathrm{f}_{\mathrm{passive}}(\lambda)$ is the passive force normalized by the maximum isometric force and it is modeled as a piecewise exponential function of the fiber stretch [6]:

$$\mathrm{f}_{\mathrm{passive}}(\lambda) = \begin{cases} 0, & \text{if } \lambda \leq \lambda_{\mathrm{opt}} \\ P_1 \left(e^{P_2(\lambda/\lambda_{\mathrm{opt}}-1)} - 1 \right), & \text{if } \lambda_{\mathrm{opt}} < \lambda < \lambda^* \\ P_3 \lambda/\lambda_{\mathrm{opt}} + P_4, & \text{if } \lambda \geq \lambda^* \end{cases} \tag{30}$$

where P_1, P_2, P_3, and P_4 are constants. Note that the values for P_3 and P_4 must preserve C^0 and C^1 continuity at $\lambda = \lambda^*$, where λ^* is the stretch above which the passive function is linear. The last term in Eq. (29) is the active force component. Specifically, $\mathrm{f}_{\mathrm{active}}(\lambda)$ is the active force normalized by the maximum isometric force and it is defined as a piecewise quadratic function of the fiber stretch [6]:

$$\mathrm{f}_{\mathrm{active}}(\lambda) = \begin{cases} 9\left(\lambda/\lambda_{\mathrm{opt}} - 0.4\right)^2, & \text{if } \lambda \leq 0.6\lambda_{\mathrm{opt}} \\ 1 - 4\left(1 - \lambda/\lambda_{\mathrm{opt}}\right)^2, & \text{if } 0.6\lambda_{\mathrm{opt}} < \lambda < 1.4\lambda_{\mathrm{opt}} \\ 9\left(\lambda/\lambda_{\mathrm{opt}} - 1.6\right)^2, & \text{if } \lambda \geq 1.4\lambda_{\mathrm{opt}} \end{cases} \tag{31}$$

2.5 Models to verify the approximation

Five models were created to validate our Ansys USERMAT subroutine that applies the approximation of the tangent modulus described in Sec. 2.3 to the hyperelastic muscle material model described in Sec. 2.4. Three “quarter-muscle” models were constructed by revolving a rectangle, a right trapezoid, and a generic obtuse trapezoid around the centerline of the muscle (Fig. 1); we refer to these models as RR, RTR, and RTO, respectively. (The dimensions of these models were based on the “Variation I” and “Variation II” models illustrated in Blemker et al. [6].) The fibers were oriented along the X-axis. All meshes were created using the “multizone” method, which

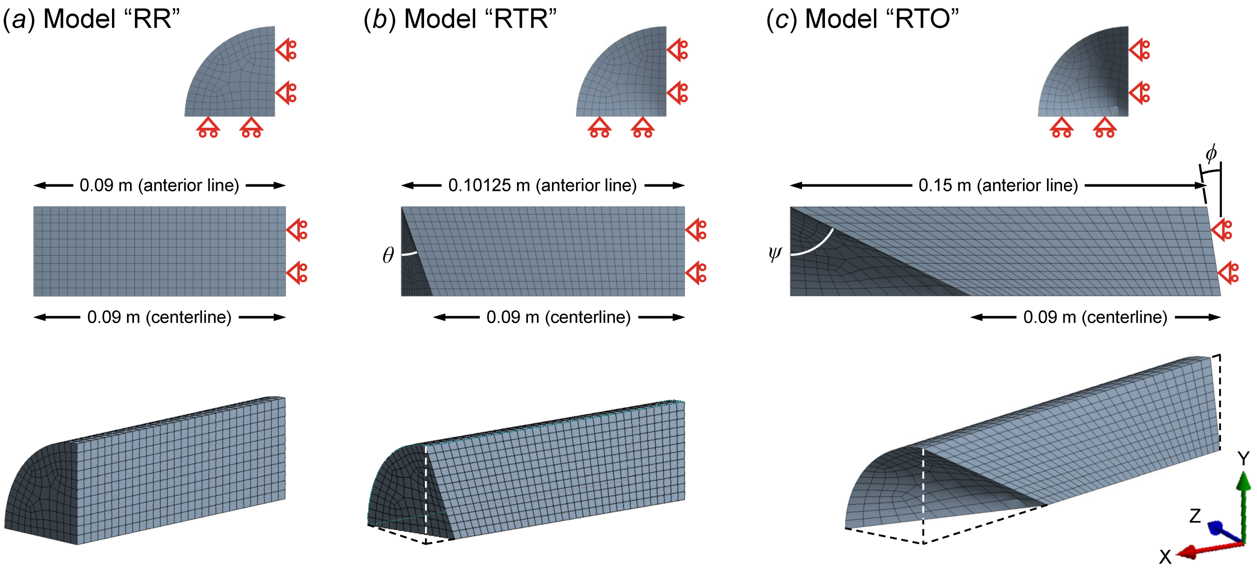

Figure 1: Models used to verify our Ansys implementation. 3D models were generated by revolving (a) a rectangle (RR), (b) a right trapezoid (RTR), and (c) an obtuse trapezoid (RTO) around the centerline. Cross-sections in the YZ-plane (top) and XY-plane (middle); 3D view (bottom). Small triangles indicate constraints on the displacement. All models have radius 0.032 m. The angles labeled in the RTR and RTO models are $\theta = 19.37°$, $\psi = 63.79°$, and $\phi = 8.88°$.

automatically decomposes the geometry into sweepable and free regions (i.e., regions in which the meshes are structured and unstructured, respectively) [41]. All models used eight-node hexahedral elements with size 0.003 m and the following constitutive parameters: $G_1 = G_2 = 50$ kPa, $\sigma_{\max} = 100\,\text{kPa}$, $\lambda^* = \lambda_{\text{opt}} = 1.4$, $\alpha = 0.15$, $P_1 = 0.05$, and $P_2 = 6.6$. Unless otherwise specified, the value of the effective bulk modulus was $K = 5.0 \times 10^5$ kPa. These parameters are similar to those used elsewhere [2,42].

To investigate the effect of element skewness along the centerline, we created two additional versions of the RTR model. Specifically, we generated models with inclination angles (θ) of 5.05° and 54.58° in addition to the "nominal" RTR model shown in Fig. 1 (where $\theta = 19.37°$) by changing the length of the anterior line, keeping the length of the centerline constant. (Note that all

Table 1: Number of elements and nodes in each model. Models were constructed by revolving a rectangle (RR), a right trapezoid (RTR), and a generic obtuse trapezoid (RTO) around the centerline of the muscle. In the RTR model, θ is the angle of the slanted face relative to vertical.

	RR	RTR ($\theta = 5.05°$)	RTR ($\theta = 19.37°$)	RTR ($\theta = 54.58°$)	RTO
Elements	3270	3379	4046	8415	3270
Nodes	4030	4160	4935	9936	4030

models, including these variants of the RTR model, have the same centerline length.) Increasing the inclination angle increases the skewness of the elements along the centerline near the slanted face. The number of elements and nodes in each model are provided in Table 1.

2.6 Simulations to verify the approximation

The models described in Sec. 2.5 were simulated by performing static analyses in Ansys. A displacement of 0.04 m was applied to the left face of each model, as shown in the middle row of Fig. 1, directed in the positive X-direction (i.e., stretching the fibers). The motion of the opposite face was constrained in the X-direction (triangles in Fig. 1, middle row). Furthermore, the motion of the faces in the XY- and XZ-planes was constrained in the direction normal to each plane (triangles in Fig. 1, top row). In Ansys, the "large deformation" option was selected and the convergence options "auto time stepping," "force convergence," and "displacement convergence" were set to "program controlled."

Simulations of the RR model were used to determine an appropriate value for the perturbation parameter (ϵ) in the approximation method. Specifically, the rate of convergence was evaluated by noting the number of iterations required to reach equilibrium when $\epsilon = 10^k$ for $k \in \{-12, -10, -8, -6, -4\}$.

To validate our results, we compared the stress and strain obtained using our implementation in Ansys with the results from analogous simulations performed in FEBio, which uses the same muscle model but with the exact value of the tangent modulus. Specifically, we compared the stress and longitudinal strain for the elements along the anterior line and centerline of each model. The stress was a direct output from Ansys and FEBio; the longitudinal strain (s) was calculated from the longitudinal deformation of each element:

$$s = \frac{L - L_0}{L_0} \tag{32}$$

where L_0 and L are the initial and final lengths of the element, respectively. Note that all models described in Sec. 2.5 have the same centerline length and are subjected to the same displacement, thus the total strain along the centerline is the same in each simulation.

We used two metrics to quantify the error between the Ansys and FEBio results. The first metric was the relative percent error (RPErr):

$$\mathrm{RPErr} = \left| \frac{\zeta_{\mathrm{FEBio}} - \zeta_{\mathrm{Ansys}}}{\zeta_{\mathrm{FEBio}}} \right| \times 100\% \tag{33}$$

where ζ is either stress or longitudinal strain. The largest RPErr for any element along either the anterior line or the centerline of the muscle (maxRPErr) was used to quantify the largest deviation between the Ansys and FEBio results. The second metric we used was the root-mean-square-percentage error (RMSPE), which quantifies the average error:

$$\mathrm{RMSPE} = \sqrt{\frac{1}{N} \sum_{k=1}^{N} \left[\left(\frac{\zeta_{\mathrm{FEBio},k} - \zeta_{\mathrm{Ansys},k}}{\zeta_{\mathrm{FEBio},k}} \times 100\% \right)^2 \right]} \tag{34}$$

where N is the number of elements along either the anterior line or the centerline.

Several authors have reported an anomalous, nonphysical growth of stress in uniaxial tests when the volumetric and isochoric components of strain energy were decoupled in isotropic materials [43] and anisotropic materials [4, 44] (Eq. (28)). Therefore, we anticipated similar behavior in our simulations. We used the $\theta = 54.58^\circ$ variant of the RTR model to explore how the effective bulk modulus (K) affects the stress and strain computed using our Ansys implementation. Specifically, we compared the longitudinal stress and longitudinal strain from simulations using four values of K: $10G_1$, 10^2G_1, 10^3G_1, and 10^4G_1.

3 Results and Discussion

3.1 Selection of the perturbation parameter

The number of iterations required to reach equilibrium at each simulation step when using the approximation of the tangent modulus is shown in Table 2. The algorithm required more iterations to achieve convergence when $\epsilon = 10^{-4}$ because, for large values of ϵ, the error of the forward difference approximation increased (Eq. (20)). On the other hand, when ϵ was very small, the perturbation approached machine precision and numerical error polluted the approximation calculation.

The Von Mises stress and the strain in the longitudinal direction were insensitive to the perturbation parameter ϵ. Stress and strain were nearly perfectly uniform across all elements of the RR model; data for one representative element are reported in Table 3. Our results agree with those reported by Sun et al. [34], who observed that the approximation for a Neo-Hookean material demonstrated the best convergence when ϵ was between 10^{-10} and 10^{-6}. Based on the observations of Sun et al. and the results shown in Tables 2 and 3, we used $\epsilon = 10^{-8}$ in the remainder of our study.

Table 2: Number of iterations required to reach equilibrium at each simulation step for different values of perturbation parameter ϵ, using the RR model. The simulation was inefficient when using the largest value of ϵ and did not converge ("DNC") when using the smallest value.

	Perturbation parameter (ϵ)				
Simulation step	10^{-12}	10^{-10}	10^{-8}	10^{-6}	10^{-4}
1	DNC	2	2	2	2
2 to 18	DNC	1	1	1	1
19	DNC	1	1	1	2
20	DNC	1	1	1	11
Total	DNC	21	21	21	32

Table 3: Sensitivity of Von Mises stress and longitudinal strain to perturbation parameter ϵ, using the RR model. Data are shown for the element along the centerline at the free end of the muscle.

	Perturbation parameter (ϵ)			
	10^{-10}	10^{-8}	10^{-6}	10^{-4}
Stress (Pa)	16494	16494	16495	16495
Strain	0.443	0.443	0.443	0.443

3.2 Simulations of the RR, RTR, and RTO models

The deformed models, shaded to visualize fiber stretch, are shown in Fig. 2. The Von Mises stress along the anterior line and centerline of each model is shown in Figs. 3(a) and 3(b), respectively. In the RR model, the Von Mises stress was constant along the entire length of the muscle, along both the anterior line and the centerline. The relative percent error (RPErr) of stress between the Ansys and FEBio solutions was 0.00% for all elements along the anterior line and centerline; the root-mean-square-percentage error (RMSPE) calculated along these lines was therefore 0.00% as well (Table 4). In the RTR model, the stress remained relatively constant for most of the length of the muscle. Specifically, for all elements from the fixed end to approximately 71% of the distance along the anterior line and centerline, the stress deviated by no more than 1.23% and 3.58% of the stress at the fixed end, respectively. Beyond 71% of the distance from the fixed end, the stress decreased by up to 21.06% and increased by up to 20.35% of the stress at the fixed end along the anterior line and centerline, respectively. The maximum RPErr (maxRPErr) of the stress over all elements along the anterior line was 3.68% (Table 4) and occurred at the free end; along the centerline, the maxRPErr was 15.09% and occurred at approximately 97% of the distance from the fixed end. In the RTO model, the stress varied along the entire anterior line. Overall, we observed good agreement between the Von Mises stress from our Ansys implementation and the analogous simulations in FEBio, except in the region near the free end along the centerline in the RTO model (Fig. 3(b)). The stress in this region increased dramatically toward the free end in both Ansys and FEBio simulations. In general, similar observations were noted for longitudinal stress, as shown in Figs. 3(c) and 3(d).

The strain from our Ansys simulations was also in good agreement with the results from FEBio; the longitudinal strain along the anterior line and centerline of each model is shown in Figs. 3(e) and 3(f), respectively. As was the case for the Von Mises and longitudinal stresses, the error in longitudinal strain was least in the RR model and greatest in the RTO model (Table 4). The peak

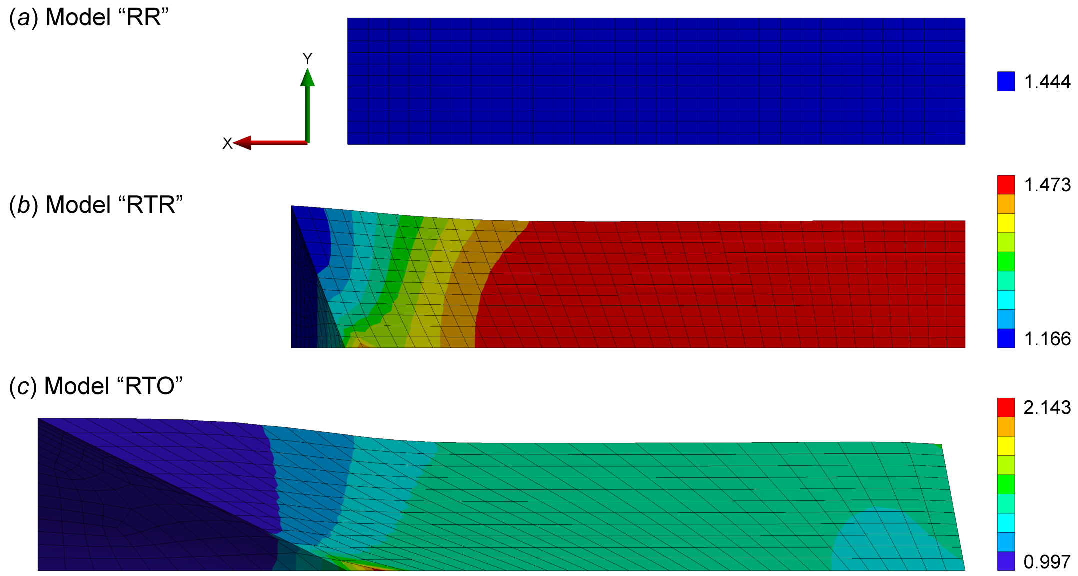

Figure 2: Visualization of fiber stretch after deformation of (a) the RR model, (b) the RTR model, and (c) the RTO model.

Table 4: Error in Von Mises stress, longitudinal stress, and longitudinal strain between Ansys and FEBio simulations for the RR, RTR, and RTO models. The maximum relative percent error (maxRPErr) and root-mean-square-percentage error (RMSPE) were calculated over the elements along the anterior line and centerline in each model.

		RR		RTR ($\theta = 19.37°$)		RTO	
		Anterior	Center	Anterior	Center	Anterior	Center
Von Mises	maxRPErr	0.00%	0.00%	3.68%	15.09%	7.47%	25.55%
Stress	RMSPE	0.00%	0.00%	0.77%	3.03%	3.08%	6.75%
Longitudinal	maxRPErr	0.00%	0.00%	2.39%	12.35%	7.01%	42.93%
Stress	RMSPE	0.00%	0.00%	0.88%	2.52%	4.88%	8.52%
Longitudinal	maxRPErr	0.00%	0.00%	3.86%	7.87%	25.63%	28.32%
Strain	RMSPE	0.00%	0.00%	1.48%	1.71%	9.52%	6.07%

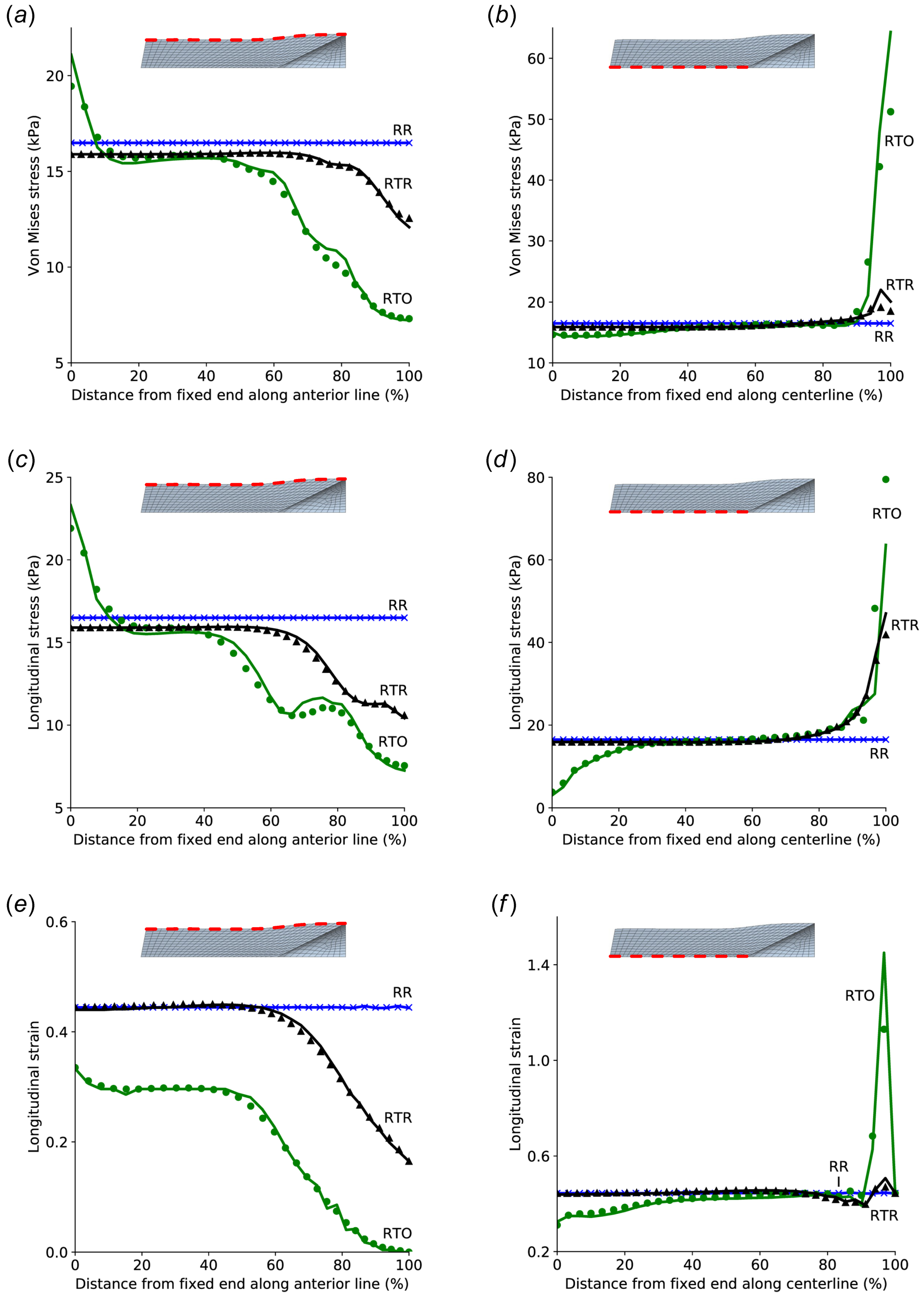

Figure 3: Stress and strain from Ansys and FEBio simulations, for elements along the length of the RR, RTR, and RTO models. Von Mises stress along (a) the anterior line and (b) the centerline; longitudinal stress along (c) the anterior line and (d) the centerline; longitudinal strain along (e) the anterior line and (f) the centerline. Results are shown from Ansys using the approximation method (solid lines) and FEBio (markers).

errors in strain generally occurred in the same regions as the peak errors in stress. In the RTO model, the strain exhibited non-smooth behavior near the free end. Note that this behavior was observed in the Ansys model as well as in the FEBio model, the latter of which uses the same muscle model but with the exact value of the tangent modulus.

3.3 Simulations of the RTR model variants

We created two additional versions of the RTR model to investigate the effect of element skewness along the centerline. The longitudinal stress along the centerline of the RTR model is shown in Fig. 4(a) for three values of inclination angle (θ; see Fig. 1): 5.05°, 19.37°, and 54.58°. The stress in the region near the fixed end was constant for all three inclination angles. At the free end of the muscle, where the elements had the greatest skewness and were closest to the applied displacement, a sharp increase in the stress was observed. This sharp increase in stress was more pronounced for higher inclination angles in both the Ansys and FEBio simulations. For the inclination angle $\theta = 54.58°$, the stress was 6.0 times larger at the free end (92.3 kPa) than at the fixed end (15.4 kPa) in the FEBio model, and was 5.4 times larger at the free end (82.3 kPa) than at the fixed end (15.2 kPa) in the Ansys model. We observed the greatest difference in stress between the Ansys and FEBio simulations with the $\theta = 54.58°$ RTR model (Table 5).

The longitudinal strain along the centerline of the RTR model is shown in Fig. 4(b) for the same three values of inclination angle (θ). The strain in the region near the fixed end was constant, with a value of 0.43 for all three inclination angles, and began decreasing at approximately 67% of the distance along the centerline. A sharp peak in strain was observed near the free end of the muscle for inclination angles of 19.37° and 54.58° in both Ansys and FEBio simulations. The largest peak occurred in the model with the greatest inclination angle, with strain reaching 3.7 and 2.6 times the strain at the fixed end in the Ansys and FEBio simulations, respectively. The difference in strain between the Ansys and FEBio simulations was largest in the $\theta = 54.58°$ RTR model (Table 5).

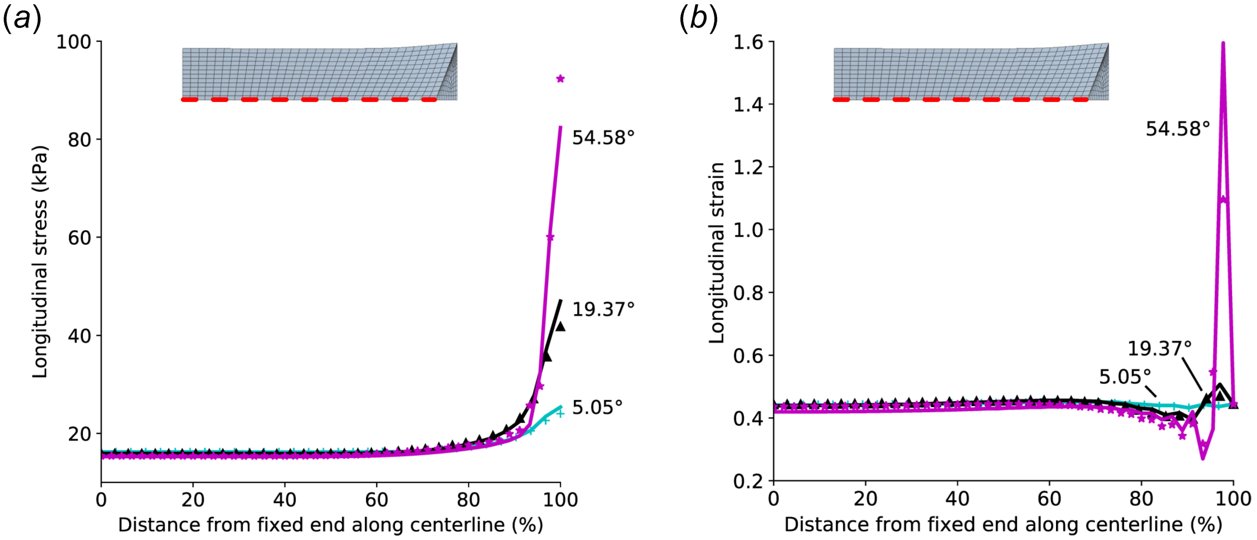

Figure 4: Longitudinal stress (a) and longitudinal strain (b) from Ansys and FEBio simulations, for elements along the centerline of the RTR model with three inclination angles (θ, as labeled). Results are shown from Ansys using the approximation method (solid lines) and FEBio (markers).

Table 5: Error in longitudinal stress and longitudinal strain between Ansys and FEBio simulations for the three variants of the RTR model. The maximum relative percent error (maxRPErr) and root-mean-square-percentage error (RMSPE) were calculated over the elements along the centerline.

		RTR ($\theta = 5.05°$)	RTR ($\theta = 19.37°$)	RTR ($\theta = 54.58°$)
Longitudinal	maxRPErr	1.23%	12.35%	14.87%
Stress	RMSPE	0.71%	2.52%	3.87%
Longitudinal	maxRPErr	0.53%	7.87%	45.60%
Strain	RMSPE	0.29%	1.71%	9.37%

The results shown in Fig. 4 support the hypothesis that element skewness contributed to the undesirable behavior observed in longitudinal stress and longitudinal strain near the free end. Recall that high longitudinal strain corresponds to high fiber stretch in this model because the fibers are oriented in the longitudinal direction. Helfenstein et al. [44] studied the behavior of fiber-reinforced, nearly incompressible materials, and noted that nonphysical responses may occur when fiber stretch is high. Specifically, they noted that elements in which the fibers dominate the calculation of total deformation energy will tend to deform in order to reduce the fiber contribution. We observed the same phenomenon in our simulations: when fiber stretch was high, the volumetric component of stress increased to nonphysical levels. As shown in Fig. 4, the peaks in stress and non-smooth behavior of strain were exacerbated by increasing element skewness in the RTR model as inclination angle increased.

3.4 Sensitivity to the effective bulk modulus

The $\theta = 54.58^\circ$ variant of the RTR model was used to explore how the effective bulk modulus (K) affects the stress and strain computed using our Ansys implementation. As shown in Fig. 5, varying K from $10G_1$ to 10^4G_1 had little effect on the longitudinal stress or longitudinal strain along the centerline from the fixed end to approximately 90% of the distance to the free end, in all simulations. In both Ansys and FEBio, the increase in stress toward the free end of the muscle was greatest when $K = 10^4G_1$ (Figs. 5(a) and 5(c)). In Ansys, the peak stress was 82.3 kPa when $K = 10^4G_1$ and 55.0 kPa when $K = 10G_1$; in FEBio, these peaks were 92.3 kPa and 71.1 kPa, respectively. The non-smooth, oscillatory behavior observed in the strain when $K = 10^4G_1$ was improved when $K = 10G_1$ in both Ansys and FEBio (Figs. 5(b) and 5(d)). In Ansys, the peak strain was 1.58 when $K = 10^4G_1$ and 1.78 when $K = 10G_1$; in FEBio, these peaks were 1.10 and 1.23, respectively. The results from Ansys and FEBio compared favorably, with maxRPErr less than 1% for stress and less than 4% for strain for the elements along the centerline from the fixed end to 90% of the distance to the free end; greater differences were observed near the free end.

Smaller values of K resulted in a lower peak longitudinal stress and smoother longitudinal strain behavior in the region near the free end. However, one must be cautious when using small values for K because the assumption of near-incompressibility may be violated. In our simulations, the volumetric ratio (J) of the element with largest peak stress and strain was 1.000, 1.002, 1.018, and 1.167 when K was 10^4, 10^3, 10^2, and 10 times the shear moduli ($G_1 = G_2$), respectively. Volumetric ratios that are substantially different from 1 suggest that the solution may be unrealistic. Thus, one must select K judiciously to find a compromise between the competing objectives of avoiding unrealistic peaks in stress and non-smooth strain behavior on one hand while respecting the incompressibility assumption on the other hand.

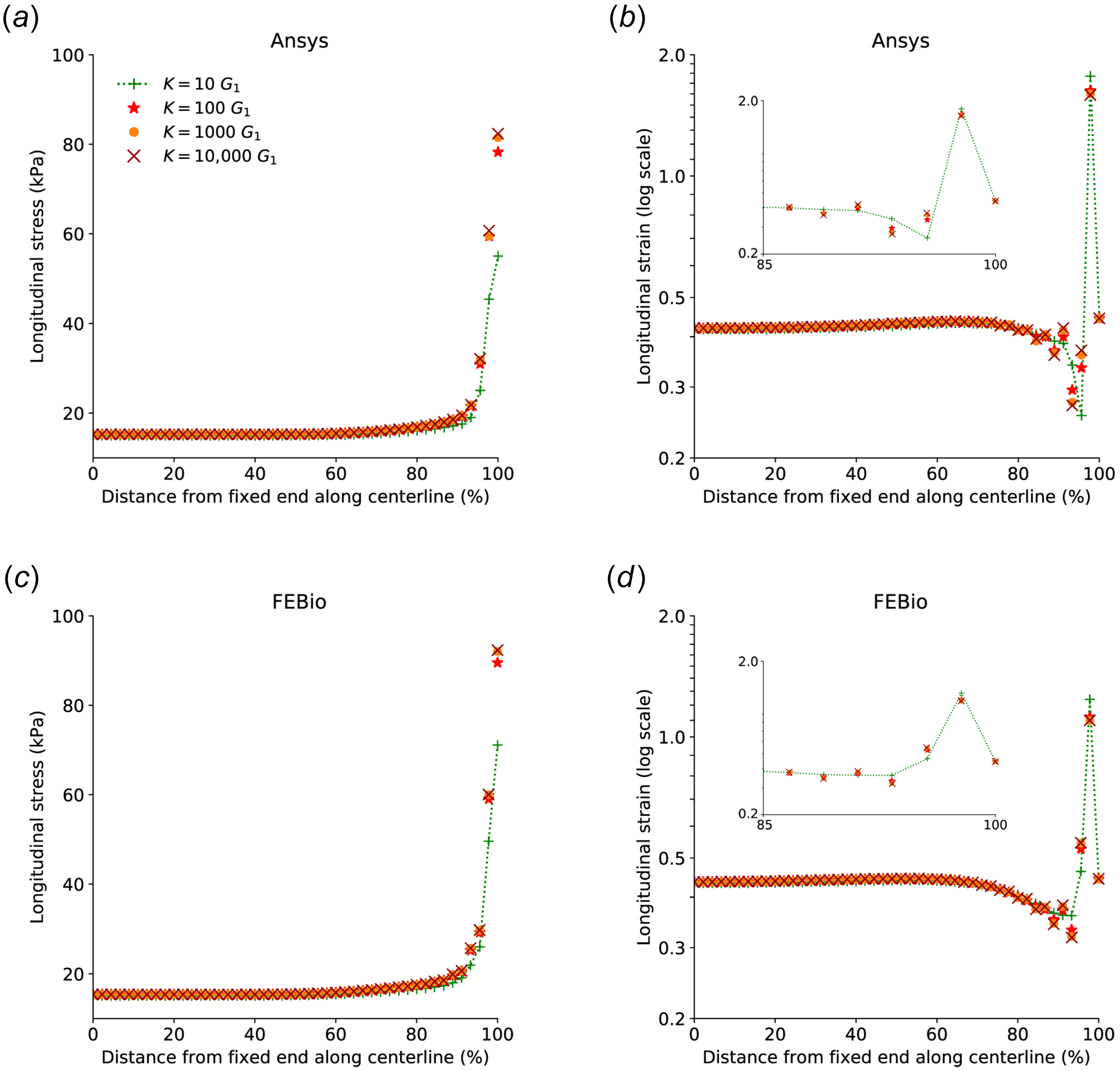

Figure 5: Longitudinal stress and longitudinal strain from Ansys ((a) and (b)) and FEBio ((c) and (d)) for elements along the centerline of the RTR model ($\theta = 54.58°$), using four values of parameter K. Insets in panels (b) and (d) magnify the plots near the free end of the muscle.

4 Conclusions

This work presents the application of an approximation for the tangent modulus based on the forward difference of the Cauchy stress [34] to a muscle material model [6]. The material model was implemented as an Ansys user-defined material subroutine and validated through comparison to analogous simulations in FEBio, which uses the same muscle model but with the exact value of the tangent modulus. Upon determining an appropriate perturbation parameter for the approximation method ($\epsilon = 10^{-8}$), we observed generally good agreement in stress and strain between Ansys and FEBio across several test scenarios, with some exceptions as noted below. Three test models were constructed by revolving a rectangle (RR), a right trapezoid (RTR), and a generic obtuse trapezoid (RTO) around the muscle's centerline. For the elements along the muscle's centerline, the root-mean-square-percentage error in the Von Mises stress was 0.00%, 3.03%, and 6.75% for the RR, RTR, and RTO models, respectively, in simulations of muscle lengthening; the corresponding errors in longitudinal strain were 0.00%, 1.71%, and 6.07%.

The effect of element skewness was tested by creating two additional versions of the RTR model with different inclination angles at the free end. The stress and strain exhibited the highest error relative to the FEBio simulations when the inclination angle was highest. Sharp increases in longitudinal stress and non-smooth behavior of longitudinal strain were observed along the muscle's centerline in the region near the free end, in both Ansys and FEBio. The largest errors in stress were also observed in this region. Smaller values of K resulted in a lower peak stress and smoother strain behavior; however, selecting a value of K that is too small will violate the assumption of near-incompressibility. Furthermore, small values of K were observed to increase the peak strain and did not entirely eliminate the nonphysical behavior of stress, which increased dramatically in the region near the free end.

The presented approximation for the tangent modulus can greatly facilitate the use of user-defined material models, as it simplifies the derivation as well as the computational implementation. In particular, programming the calculation of stress in the co-rotational frame is much easier using the approximation method than directly evaluating the exact tangent modulus tensor. In this work, we observed an expected but mild reduction in accuracy when using the approximation method, with the error increasing as element skewness increased. Based on these results, and noting that the approximation method is independent of the specific material model that is used, we recommend applying the approximation to other materials to simplify implementation.

There are two key limitations of this work. First, the test cases we explored use relatively simple geometry. Using simple geometry facilitated thorough analysis and will allow others to easily reproduce our test cases. In future work, more complex geometry will be used to explore the effect of the tangent modulus approximation in more realistic scenarios. Second, we compared the stress and strain in our Ansys simulations to analogous simulations in FEBio. Some of the error in our test cases is likely to have resulted from inherent differences between Ansys and FEBio rather than from the approximation of the tangent modulus itself—though we do not expect software-dependent differences to play a substantial role in all conditions since the relative error in stress and strain was 0.00% for the RR model. We have provided our Ansys implementation and usage notes at https://simtk.org/projects/musc_fe_approx so that others can reproduce and extend our results, use the model in their own finite element simulations, and develop new muscle material models in Ansys more quickly.

Funding Statement

This work was supported by the Natural Sciences and Engineering Research Council of Canada (RGPIN-2019-05726 [T.K.U.]). The funders had no role in study design, data collection and analysis, decision to publish, or preparation of the manuscript.

References

[1] Wang, Y., Downie, S., Wood, N., Firmin, D., and Xu, X. Y., 2013. “Finite element analysis of the deformation of deep veins in the lower limb under external compression”. *Med. Eng. Phys.,* **35**(4), pp. 515–523. doi:10.1016/j.medengphy.2012.06.019.

[2] Rehorn, M. R., and Blemker, S. S., 2010. “The effects of aponeurosis geometry on strain injury susceptibility explored with a 3D muscle model”. *J. Biomech.,* **43**(13), pp. 2574–2581. doi:10.1016/j.jbiomech.2010.05.011.

[3] Böl, M., and Reese, S., 2008. “Micromechanical modelling of skeletal muscles based on the finite element method”. *Comput. Methods Biomech. Biomed. Eng.,* **11**(5), pp. 489–504. doi:10.1080/10255840701771750.

[4] Weickenmeier, J., Itskov, M., Mazza, E., and Jabareen, M., 2014. “A physically motivated constitutive model for 3D numerical simulation of skeletal muscles”. *Int. J. Numer. Methods Biomed. Eng.,* **30**(5), pp. 545–562. doi:10.1002/cnm.2618.

[5] Röhrle, O., Davidson, J. B., and Pullan, A. J., 2008. “Bridging scales: a three-dimensional electromechanical finite element model of skeletal muscle”. *SIAM J. Sci. Comput.,* **30**(6), pp. 2882–2904. doi:10.1137/070691504.

[6] Blemker, S. S., Pinsky, P. M., and Delp, S. L., 2005. “A 3D model of muscle reveals the causes of nonuniform strains in the biceps brachii”. *J. Biomech.,* **38**(4), pp. 657–665. doi:10.1016/j.jbiomech.2004.04.009.

[7] Oomens, C. W. J., Maenhout, M., van Oijen, C. H., Drost, M. R., and Baaijens, F. P., 2003. “Finite element modelling of contracting skeletal muscle”. *Philos. Trans. R. Soc. Lond. B Biol. Sci.,* **358**(1437), pp. 1453–1460. doi:10.1098/rstb.2003.1345.

[8] Dao, T. T., and Tho, M.-C. H. B., 2018. "A systematic review of continuum modeling of skeletal muscles: current trends, limitations, and recommendations". *Appl. Bionics Biomech.,* **2018**, p. 7631818. doi:10.1155/2018/7631818.

[9] Hill, A. V., 1938. "The heat of shortening and the dynamic constants of muscle". *Proc. R. Soc. Lond. B Biol. Sci.,* **126**(843), pp. 136–195. doi:10.1098/rspb.1938.0050.

[10] Uchida, T. K., and Delp, S. L., 2021. *Biomechanics of Movement: The Science of Sports, Robotics, and Rehabilitation.* The MIT Press, Cambridge, MA.

[11] Hernández-Gascón, B., Grasa, J., Calvo, B., and Rodríguez, J. F., 2013. "A 3D electro-mechanical continuum model for simulating skeletal muscle contraction". *J. Theor. Biol.,* **335**, pp. 108–118. doi:10.1016/j.jtbi.2013.06.029.

[12] Böl, M., Weikert, R., and Weichert, C., 2011. "A coupled electromechanical model for the excitation-dependent contraction of skeletal muscle". *J. Mech. Behav. Biomed. Mater.,* **4**(7), pp. 1299–1310. doi:10.1016/j.jmbbm.2011.04.017.

[13] Huxley, A. F., 1957. "Muscle structure and theories of contraction". *Prog. Biophys. Biophys. Chem.,* **7**, pp. 255–318. doi:10.1016/s0096-4174(18)30128-8.

[14] Beldie, L., Walker, B., Lu, Y., Richmond, S., and Middleton, J., 2010. "Finite element modelling of maxillofacial surgery and facial expressions – a preliminary study". *Int. J. Med. Robot.,* **6**(4), pp. 422–430. doi:10.1002/rcs.352.

[15] Calvo, B., Ramírez, A., Alonso, A., Grasa, J., Soteras, F., Osta, R., and Muñoz, M. J., 2010. "Passive nonlinear elastic behaviour of skeletal muscle: experimental results and model formulation". *J. Biomech.,* **43**(2), pp. 318–325. doi:10.1016/j.jbiomech.2009.08.032.

[16] Ehret, A. E., and Itskov, M., 2007. "A polyconvex hyperelastic model for fiber-reinforced materials in application to soft tissues". *J. Mater. Sci.,* **42**(21), pp. 8853–8863. doi:10.1007/s10853-007-1812-6.

[17] Hedenstierna, S., and Halldin, P., 2008. "How does a three-dimensional continuum muscle model affect the kinematics and muscle strains of a finite element neck model compared to a discrete muscle model in rear-end, frontal, and lateral impacts". *Spine,* **33**(8), pp. E236–E245. doi:10.1097/brs.0b013e31816b8812.

[18] Zöllner, A. M., Pok, J. M., McWalter, E. J., Gold, G. E., and Kuhl, E., 2015. "On high heels and short muscles: a multiscale model for sarcomere loss in the gastrocnemius muscle". *J. Theor. Biol.,* **365**, pp. 301–310. doi:10.1016/j.jtbi.2014.10.036.

[19] Büchler, P., Ramaniraka, N. A., Rakotomanana, L. R., Iannotti, J. P., and Farron, A., 2002. "A finite element model of the shoulder: application to the comparison of normal and osteoarthritic joints". *Clin. Biomech.,* **17**(9–10), pp. 630–639. doi:10.1016/s0268-0033(02)00106-7.

[20] Barbarino, G. G., Jabareen, M., Trzewik, J., Nkengne, A., Stamatas, G., and Mazza, E., 2009. "Development and validation of a three-dimensional finite element model of the face". *J. Biomech. Eng.,* **131**(4), p. 041006. doi:10.1115/1.3049857.

[21] Ehret, A. E., Böl, M., and Itskov, M., 2011. "A continuum constitutive model for the active behaviour of skeletal muscle". *J. Mech. Phys. Solids,* **59**(3), pp. 625–636. doi:10.1016/j.jmps.2010.12.008.

[22] Grasa, J., Ramírez, A., Osta, R., Muñoz, M. J., Soteras, F., and Calvo, B., 2011. "A 3D active-passive numerical skeletal muscle model incorporating initial tissue strains. Validation with

experimental results on rat tibialis anterior muscle". *Biomech. Model. Mechanobiol.,* **10**(5), pp. 779–787. doi:10.1007/s10237-010-0273-z.

[23] Li, J., Lu, Y., Miller, S. C., Jin, Z., and Hua, X., 2019. "Development of a finite element musculoskeletal model with the ability to predict contractions of three-dimensional muscles". *J. Biomech.,* **94**, pp. 230–234. doi:10.1016/j.jbiomech.2019.07.042.

[24] Tang, C. Y., Zhang, G., and Tsui, C. P., 2009. "A 3D skeletal muscle model coupled with active contraction of muscle fibres and hyperelastic behaviour". *J. Biomech.,* **42**(7), pp. 865–872. doi:10.1016/j.jbiomech.2009.01.021.

[25] Li, F., Li, H., Hu, W., Su, S., and Wang, B., 2016. "Simulation of muscle activation with coupled nonlinear FE models". *J. Mech. Med. Biol.,* **16**(6), p. 1650082. doi:10.1142/s0219519416500822.

[26] Maas, S. A., Ellis, B. J., Ateshian, G. A., and Weiss, J. A., 2012. "FEBio: finite elements for biomechanics". *J. Biomech. Eng.,* **134**(1), p. 011005. doi:10.1115/1.4005694.

[27] Maas, S. A., Ateshian, G. A., and Weiss, J. A., 2017. "FEBio: history and advances". *Annu. Rev. Biomed. Eng.,* **19**, pp. 279–299. doi:10.1146/annurev-bioeng-071516-044738.

[28] Scherb, D., Wartzack, S., and Miehling, J., 2023. "Modelling the interaction between wearable assistive devices and digital human models—a systematic review". *Front. Bioeng. Biotechnol.,* **10**, p. 1044275. doi:10.3389/fbioe.2022.1044275.

[29] Yandell, M. B., Quinlivan, B. T., Popov, D., Walsh, C., and Zelik, K. E., 2017. "Physical interface dynamics alter how robotic exosuits augment human movement: implications for optimizing wearable assistive devices". *J. Neuroeng. Rehabil.,* **14**(1), p. 40. doi:10.1186/s12984-017-0247-9.

[30] Holzapfel, G. A., 2000. *Nonlinear Solid Mechanics: A Continuum Approach for Engineering*. John Wiley & Sons, Chichester, England.

[31] Cheng, J., and Zhang, L. T., 2018. "A general approach to derive stress and elasticity tensors for hyperelastic isotropic and anisotropic biomaterials". *Int. J. Comput. Methods,* **15**(4), p. 1850028. doi:10.1142/s0219876218500287.

[32] ANSYS Inc., 2013. ANSYS Mechanical APDL Technology Demonstration Guide, Release 15.0. Tech. rep., Canonsburg, PA, November 2013.

[33] Miehe, C., 1996. "Numerical computation of algorithmic (consistent) tangent moduli in large-strain computational inelasticity". *Comput. Methods Appl. Mech. Eng.,* **134**(3–4), pp. 223–240. doi:10.1016/0045-7825(96)01019-5.

[34] Sun, W., Chaikof, E. L., and Levenston, M. E., 2008. "Numerical approximation of tangent moduli for finite element implementations of nonlinear hyperelastic material models". *J. Biomech. Eng.,* **130**(6), p. 061003. doi:10.1115/1.2979872.

[35] Tanaka, M., and Fujikawa, M., 2011. "Numerical approximation of consistent tangent moduli using complex-step derivative and its application to finite deformation problems". *Trans. Jpn. Soc. Mech. Eng. A,* **77**(773), pp. 27–38.

[36] Suchocki, C., 2011. "A finite element implementation of Knowles stored-energy function: theory, coding and applications". *Arch. Mech. Eng.,* **58**(3), pp. 319–346. doi:10.2478/v10180-011-0021-7.

[37] Gasser, T. C., Ogden, R. W., and Holzapfel, G. A., 2006. "Hyperelastic modelling of arterial layers with distributed collagen fibre orientations". *J. R. Soc. Interface,* **3**(6), pp. 15–35. doi:10.1098/rsif.2005.0073.

[38] Liu, H., and Sun, W., 2017. "Numerical approximation of elasticity tensor associated with Green-Naghdi rate". *J. Biomech. Eng.,* **139**(8), p. 081007. doi:10.1115/1.4036829.

[39] Fehervary, H., Maes, L., Vastmans, J., Kloosterman, G., and Famaey, N., 2020. "How to implement user-defined fiber-reinforced hyperelastic materials in finite element software". *J. Mech. Behav. Biomed. Mater.,* **110**, p. 103737. doi:10.1016/j.jmbbm.2020.103737.

[40] Liu, H., and Sun, W., 2016. "Computational efficiency of numerical approximations of tangent moduli for finite element implementation of a fiber-reinforced hyperelastic material model". *Comput. Methods Biomech. Biomed. Eng.,* **19**(11), pp. 1171–1180. doi:10.1080/10255842.2015.1118467.

[41] ANSYS Inc., 2010. ANSYS Meshing User's Guide, Release 13.0. Tech. rep., Canonsburg, PA, November 2010.

[42] Fiorentino, N. M., and Blemker, S. S., 2014. "Musculotendon variability influences tissue strains experienced by the biceps femoris long head muscle during high-speed running". *J. Biomech.,* **47**(13), pp. 3325–3333. doi:10.1016/j.jbiomech.2014.08.010.

[43] Ehlers, W., and Eipper, G., 1998. "The simple tension problem at large volumetric strains computed from finite hyperelastic material laws". *Acta Mech.,* **130**(1), pp. 17–27. doi:10.1007/bf01187040.

[44] Helfenstein, J., Jabareen, M., Mazza, E., and Govindjee, S., 2010. "On non-physical response in models for fiber-reinforced hyperelastic materials". *Int. J. Solids Struct.,* **47**(16), pp. 2056–2061. doi:10.1016/j.ijsolstr.2010.04.005.